Earth, Planets and Space

FULL PAPER Open Access

Stabilizing REGARD with real-time MCMC uncertainty quantification and precise point positioning

Keitaro Ohno[1*], Satoshi Abe[1], Naofumi Takamatsu[1], Takayuki Miyazaki[1], Koki Yoshinaga[1], Chinami Shodai[1], Mayumi Hashimoto[1], Riku Yamamoto[1], Satoshi Kawamoto[1] and Yusaku Ohta[2,3,4,5]

Abstract

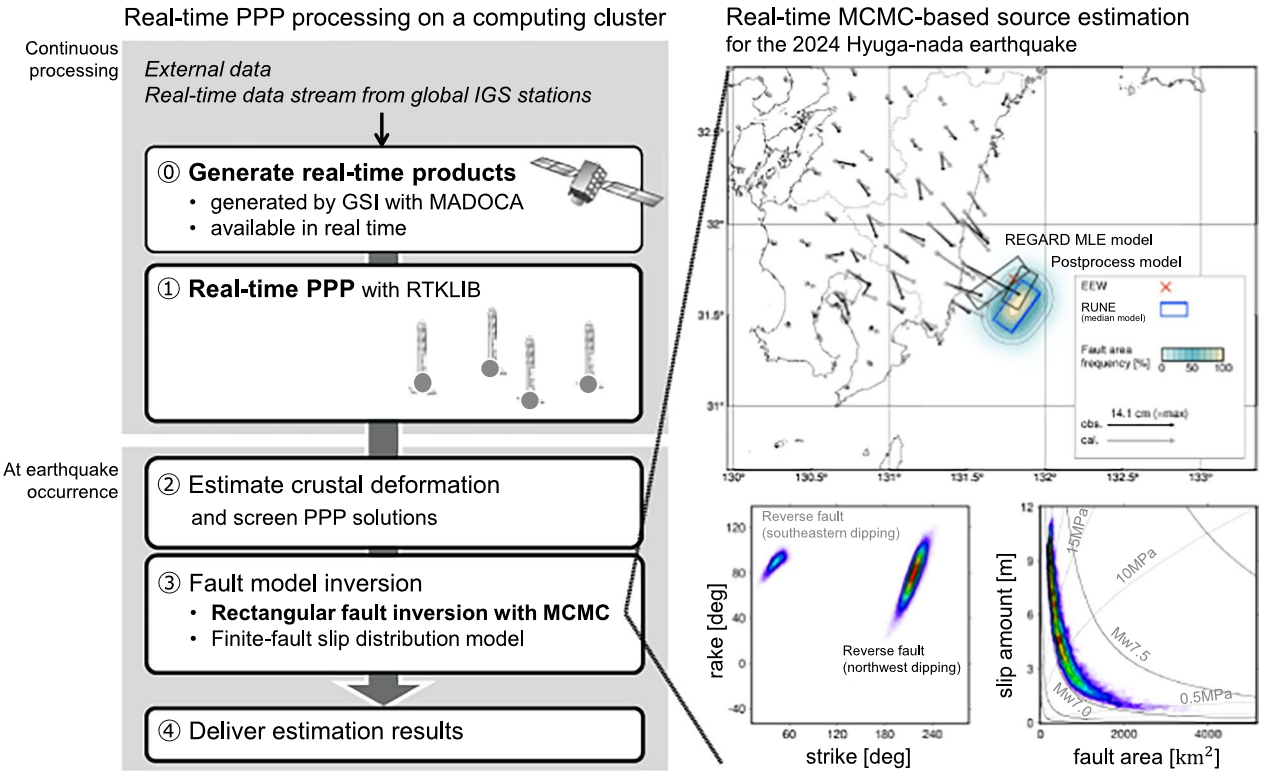
This study introduces structural upgrades to REGARD, Japan's real-time GNSS-based coseismic analysis system, addressing two long-standing limitations in real-time geodetic source modeling: the absence of explicit uncertainty quantification in fault estimates and positioning instability due to reference-station dependence. These limitations reduce the reliability and physical interpretability of automated products used for rapid earthquake and tsunami assessments. To quantify uncertainty under strict real-time constraints, we implement a Bayesian inversion framework based on Markov chain Monte Carlo (MCMC), termed RUNE, for estimating a single rectangular fault model. RUNE outputs posterior probability density functions for moment magnitude (Mw) and fault parameters. Stable and efficient operation is achieved through physically informed priors and likelihood regularization through variance lower bounds designed to ensure statistical consistency, thereby suppressing noise-driven overfitting while retaining sensitivity to genuine crustal deformation. To improve positioning robustness, we introduce a real-time precise point positioning (PPP) cluster that eliminates reference-station dependence and mitigates network-wide translational artifacts inherent in real-time kinematic (RTK) positioning. Additional procedures—automatic station screening based on per-epoch position uncertainty and removal of common-mode trends estimated from distant stations—further stabilize displacement fields and improve the validity of the statistical assumptions used in Bayesian inversion. Applications to recent Japanese earthquakes, including the 2024 Noto Peninsula and Hyuga-nada events, together with 5 years of operational statistics, demonstrate that the combined MCMC–PPP upgrades markedly reduce false alarms while remaining consistent with post-processed solutions. Overall, the introduction of explicit uncertainty quantification and stabilized real-time positioning enhances the reliability and interpretability of automated GNSS-based coseismic source modeling for rapid hazard assessment.

Keywords GNSS coseismic displacement, Real-time geodesy, Bayesian inversion, Uncertainty quantification, Markov chain Monte Carlo (MCMC), Precise point positioning (PPP), REGARD system, Earthquake source modeling, Coseismic fault estimation, Real-time hazard assessment

*Correspondence:
Keitaro Ohno
ohno-k96pi@mlit.go.jp
Full list of author information is available at the end of the article

© The Author(s) 2026. **Open Access** This article is licensed under a Creative Commons Attribution 4.0 International License, which permits use, sharing, adaptation, distribution and reproduction in any medium or format, as long as you give appropriate credit to the original author(s) and the source, provide a link to the Creative Commons licence, and indicate if changes were made. The images or other third party material in this article are included in the article's Creative Commons licence, unless indicated otherwise in a credit line to the material. If material is not included in the article's Creative Commons licence and your intended use is not permitted by statutory regulation or exceeds the permitted use, you will need to obtain permission directly from the copyright holder. To view a copy of this licence, visit http://creativecommons.org/licenses/by/4.0/.

Graphical Abstract



1 Introduction

High-rate Global Navigation Satellite System (GNSS) analyses have enabled detailed characterization of crustal deformation on sub-daily to near-instantaneous time scales. Building on these advances, real-time GNSS-based crustal-deformation analysis has been actively developed to rapidly assess earthquake disasters (e.g., Larson et al. 2003; Ohta et al. 2006, 2012; Larson 2009; Blewitt et al. 2006, 2009; Melgar et al. 2012, 2016; Melgar and Bock 2013; Tanaka et al. 2019). REGARD (Real-time GEONET Analysis system for Rapid Deformation monitoring), jointly developed by the Geospatial Information Authority of Japan (GSI) and Tohoku University, is a real-time GNSS analysis system in Japan. The system uses the GNSS Earth Observation Network System (GEONET), the nationwide GNSS network operated by GSI, and estimates earthquake magnitude by inverting coseismic GNSS displacements to derive coseismic fault models (Kawamoto et al. 2016, 2017; Ohno et al. 2021, 2022, 2024a). Conventional post-processing workflows for disaster response typically require several hours to calculate coseismic deformation and invert for fault models. In contrast, REGARD processes GEONET data in real time and provides fault-model estimates within approximately 10 min of an earthquake. These products are employed by national agencies for rapid hazard assessment; for example, they are used as reference information for updated tsunami warnings issued by the Japan Meteorological Agency (JMA) and as input to the Cabinet Office's real-time tsunami inundation and damage-mapping system (Ohta et al. 2018). GNSS-based rapid source-characterization systems have been developed not only in Japan but also in the United States (G-FAST and G-larmS; Murray et al. 2019; Ruhl et al. 2019) and in Chile, New Zealand, and Taiwan (e.g., Báez et al. 2018; Lin et al. 2019; Kaiser et al. 2024). Nevertheless, Japan is unique in terms of GNSS station density and the high frequency of earthquakes (e.g., Sagiya 2004; Tsuji and Hatanaka 2018; Ruhl et al. 2019). Accordingly, REGARD has accumulated one of the world's most extensive records of operational experience.

Despite its achievements, several challenges remain in REGARD's operational performance. First, uncertainties in the estimated fault parameters arising from observational and modeling errors, such as those associated with the Green's functions, have not yet been systematically

quantified. REGARD currently estimates a single rectangular fault model by solving a nonlinear inverse problem using maximum-likelihood estimation (MLE). In practice, the conventional approach (Matsu'ura and Hasegawa, 1987) is known to be highly sensitive to the choice of initial values and prone to convergence to local minima. During the 2016 Kumamoto earthquake, the inversion became trapped on a conjugate fault near the initial strike, which substantially increased the computation time before convergence to the correct fault strike (Kawamoto et al. 2016). The variability derived from such an MLE-based procedure reflects only the local behavior around the obtained solution (i.e., the local curvature of the likelihood surface) and, therefore, does not represent the full range of fault parameters consistent with observational and modeling errors. Reporting the output of an automated analysis system as a single deterministic estimate, therefore, risks conveying a level of certainty that exceeds the system's actual resolving power. Accordingly, it is desirable for REGARD to autonomously provide quantitative uncertainty measures for its estimated parameters.

The second issue is that the noise characteristics of the real-time kinematic (RTK) positioning used in REGARD's positioning subsystem can compromise the stability of the inversion subsystem. REGARD currently performs RTK positioning using a single reference station (Kawamoto et al. 2017), meaning that observation or analysis errors at the reference site can propagate coherently to all baselines (Ohta et al. 2012). In real-time source modeling, the estimation must be completed under strict computational and a priori constraints without manual intervention. The inversion assumes Gaussian positioning errors with zero-mean residuals. However, such coherent network-wide bias in RTK positioning violates the zero-mean assumption and leads to non-Gaussian residuals. As a result, these biases may be misinterpreted as apparent crustal deformation.

In operational use, we identified a "false alarm," wherein a physically implausible fault model was estimated when network-wide translational noise dominated the displacement field. The inversion results are evaluated using the variance reduction (VR), defined in the following equation:

$$VR = 100\left(1 - \frac{\boldsymbol{r}^T\boldsymbol{r}}{\boldsymbol{d}^T\boldsymbol{d}}\right), \tag{1}$$

where $\boldsymbol{r}^T\boldsymbol{r}$ and $\boldsymbol{d}^T\boldsymbol{d}$ denote the residual sum of squares and the data sum of squares for the three-dimensional displacements, respectively. Following Kawamoto et al. (2017), models with VR $\geq$ 80% are regarded as reliable. However, VR does not account for data reliability and can be artificially high in noise-dominated cases, leading to overfitting. In this study, we define such cases—where VR exceeds 80% primarily due to noise rather than genuine crustal deformation—as false alarms. In this paper, a "false alarm" does not refer to incorrect earthquake detection itself, but to cases in which the inversion produces a physically implausible fault model from noise-dominated displacement data. To reduce the risk of false alarms, REGARD employs three clusters, in which all stations are processed using different reference stations and automatically selects the best result; however, this approach does not fundamentally eliminate the problem. Based on operational records since 2016, 99% of the events triggered by REGARD have occurred under low signal-to-noise conditions in which no crustal deformation was detected. In other words, the majority of triggered events correspond to noise-dominated cases rather than genuine deformation signals. Therefore, the primary challenge in routine operation is to avoid false alarms under such noise-dominated conditions. Improving the stability of positioning errors is thus directly linked to enhancing the operational stability of the system.

To address these challenges, we develop an operationally feasible Bayesian inversion framework that maintains probabilistic rigor while ensuring computational stability in real-time applications. Specifically, we develop and implement an algorithm that enables real-time Markov chain Monte Carlo (MCMC) source inversion. In addition, we report integrated system improvements, including the introduction of real-time precise point positioning (PPP), which reduces network-wide errors associated with reference-station dependence and makes the residuals more consistent with the zero-mean Gaussian assumption.

2 Methods

2.1 Introduction of MCMC

This section explains the motivation for introducing MCMC in place of MLE for estimating a rectangular fault model and describes the resulting operational framework. We formulate the real-time fault estimation problem as a Bayesian inverse problem. The observed displacement vector $\boldsymbol{d}$ is related to the model parameters $\boldsymbol{\theta}$ through a forward model:

$$\boldsymbol{d} = G(\boldsymbol{\theta}) + \boldsymbol{\varepsilon}, \tag{2}$$

where $\boldsymbol{\theta}$ includes the fault parameters (latitude, longitude, depth, strike, dip, rake, length, width, slip amount), and $G(\boldsymbol{\theta})$ represents the predicted displacement and $\boldsymbol{\varepsilon}$ denotes observation errors, which are assumed to follow a zero-mean Gaussian distribution with variance $\sigma_i^2 (i = horizontal(EN), vertical(U))$. The likelihood function is expressed as

$$p(\boldsymbol{d}|\boldsymbol{\theta}) = \prod_{i=EN,\,U} \frac{1}{\sqrt{\left(2\pi\sigma_i^2\right)^{N_i}}} \exp\left[-\frac{1}{2\sigma_i^2}\boldsymbol{r}_i^T\boldsymbol{r}\right], \quad (3)$$

and the posterior distribution is given by

$$p(\boldsymbol{\theta}|\boldsymbol{d}) \propto p(\boldsymbol{d}|\boldsymbol{\theta})\, p(\boldsymbol{\theta}), \quad (4)$$

where N_i denotes the number of observations, and σ_i represents the effective data noise level, including modeling errors. Based on this formulation, we developed the RUNE algorithm (Real-time automatic uncertainty estimation of source models using crustal-deformation data) (Ohno et al. 2021, 2024a). RUNE employs a Metropolis–Hastings sampler (Metropolis 1953; Hastings 1970) with parallel tempering (Geyer 1991; Jasra et al. 2007), running eight chains to infer the posterior probability density functions (PDFs) of the parameters of a single-rectangular fault model (Okada 1992). RUNE emphasizes real-time MCMC automation, with the key feature of automatically estimating σ while incorporating modeling errors. While previous studies have highlighted the importance of treating modeling errors more rigorously (e.g., Ragon et al. 2018; Agata et al. 2021), our approach adopts a simplified treatment to ensure robustness and computational efficiency in real-time applications. Specifically, σ is estimated from the approximation error associated with the single-rectangular fault model in the maximum-likelihood framework (e.g., Dettmer et al. 2014), providing a practical representation of combined observational and modeling uncertainties.

The mathematical formulation of RUNE has been described in detail by Ohno et al. (2021, 2024a). Therefore, we do not repeat those derivations here; instead, we focus on the modifications and tuning required to ensure stable operation within the operational REGARD environment. In particular, the algorithm must remain stable under noise-dominated conditions, avoiding divergence or convergence to physically implausible, excessively large fault models while still converging rapidly under genuine crustal deformation.

To ensure stable Bayesian inference under real-time constraints, we adopted four design principles: (1) restricting exploration to physically plausible regions of the parameter space, (2) preventing unrealistically small variance estimates in the likelihood function, (3) maintaining computational feasibility within a fixed time window, and (4) ensuring computationally efficient and stable evaluation of required statistical quantities. Together, these principles define the core requirements for real-time probabilistic inversion, independent of specific parameter choices. They are implemented through the following mechanisms.

2.1.1 Prior PDFs design

First, we redesigned the prior PDF for fault geometry from Ohno et al. (2021), particularly for strike angle, which can be poorly constrained when observational data are limited. To restrict parameter exploration to a more realistic domain, we incorporated the focal-mechanism catalog used in REGARD's MLE procedure (Kawamoto et al. 2017) as prior information. For each spatial grid, the catalog provides two conjugate nodal planes. Accordingly, we assigned a bimodal prior distribution with two peaks corresponding to these planes while allowing non-zero probability over a broader range of orientations. Specifically, the prior takes a lower bound of 0.66 relative to the peak (Fig. S1). The prior PDFs for the other fault parameters follow Ohno et al. (2021). The prior PDFs for dip and rake angles are modeled as uniform distributions rather than bimodal distributions. Fault length and width are constrained using a scaling law based on the Earthquake Early Warning (EEW) magnitude M_{eew}, which is implemented as a trigger for execution of the subsequent inversion. In contrast, no magnitude-dependent constraints are imposed on slip amount, so that the Mw is primarily determined by the likelihood when significant deformation is observed. Overall, the prior design aims to provide physically informed constraints while allowing the data to drive the posterior distribution where observational information is sufficient, avoiding overly restrictive assumptions on earthquake size or fault geometry to maintain flexibility for unanticipated events.

2.1.2 Likelihood regularization

Second, we imposed lower bounds on the standard deviation, σ, in the likelihood function (Eq. 3). Here, σ represents the combined level of observational and modeling errors. When substantial deformation is observed at only a few stations or when non-Gaussian noise dominates (e.g., network-wide translational artifacts or isolated outliers), the effective noise level may be underestimated, as σ is inferred within a maximum-likelihood framework based on the single-rectangular fault model. This can cause σ to fall below the typical GNSS noise level and lead to overfitting. To mitigate this effect, we imposed σ floors of 1.5 cm for the horizontal component and 2.0 cm for the vertical component. These thresholds approximate the minimum resolvable deformation scale of GEONET under real-time conditions and prevent likelihood degeneracy in low signal-to-noise situations. The values were derived from 5 years of operational statistics and represent the lower envelope of steady-state positioning errors together with residual modeling errors associated with the single-rectangular-fault approximation. This constraint can influence the relative preference

between conjugate solutions and the inferred magnitude range when deformation amplitudes are close to these thresholds (Fig. S2).

2.1.3 Computational constraints

Third, we fixed the MCMC sampling budget. The inversion uses eight parallel-tempering chains, each generating 4×10^6 samples. REGARD updates crustal-deformation estimates and executes the inversion every 10 s within a 5 min processing window. The sampling budget was selected to satisfy this operational requirement on the deployed Linux servers (e.g., Intel Xeon 3.0 GHz CPUs with 24 cores and 48 threads), based on extensive testing using 5 years of operational logs and accounting for acceptance rates and replica-exchange behavior. To minimize computational overhead, posterior PDF visualization and other diagnostic plots are generated only once per trigger, using the sample set from the model that achieves the highest VR after all inversion cycles are completed.

2.1.4 Statistical value calculation

Fourth, we define a set of statistical procedures. REGARD reports representative solutions using the median of each posterior PDF as the point estimate. Uncertainty is summarized using the 95% confidence interval (CI) and the posterior range (minimum–maximum) for each parameter. For cyclic parameters, such as strike and rake, a naive median can be misleading when samples straddle the 0°/360° (or ± 180°) boundary. To obtain a meaningful estimate, we circularly shift the samples with respect to the dominant mode and then compute the median in the shifted domain. When the posterior PDF is strongly multimodal, a single median may not adequately represent the solution. Therefore, REGARD also provides multiple representative models (e.g., the posterior mean, posterior mode, and the model with the highest VR) together with marginal PDFs for operational review. These additional products can also be distributed externally when necessary. Overall, these procedures provide relevant agencies with model estimates accompanied by quantitative uncertainty, rather than a single deterministic solution.

2.2 Introduction of real-time PPP

Reliance on a single reference station introduces network-wide translational noise that violates the statistical assumptions underlying Bayesian inversion, particularly the assumption of zero-mean residuals. To address this issue, we introduce PPP as a structural modification to the positioning subsystem. Because PPP does not require reference stations (Zumberge et al. 1997; Kouba and Héroux 2001), it avoids the translational errors inherent in RTK and better satisfies the commonly assumed inter-station independence in geodetic likelihood formulations. In REGARD, RTK-specific errors have been mitigated using multiple reference-station clusters; however, the removal of reference-station dependence in PPP reduces the need for such redundancy, potentially lowering system complexity and computational cost. This section describes the operational architecture used to implement real-time PPP in REGARD.

The GSI and the Japan Aerospace Exploration Agency (JAXA) operate the IGS Analysis Center "JGX", which produces post-processed precise GNSS orbit and clock products (Ohno et al. 2024b). As part of that project, we generate real-time GNSS orbit and clock products using MADOCA (Kawate et al. 2023). By applying the MADOCA products, we calculate 1-Hz GEONET station coordinates in real time.

Figure 1 illustrates the PPP processing workflow in comparison with conventional RTK processing. We introduced real-time PPP as a fourth processing cluster in addition to the three redundant RTK clusters used in the original system. Compared with the RTK clusters, the PPP cluster differs primarily in that its real-time processing includes an additional preprocessing stage (*Step 0*). In *Step 0*, the precise orbit and clock estimation subsystem ingests real-time observation streams from approximately 120 IGS stations via multiple data providers (e.g., MIRAI, IGS-IP, and EUREF-IP) and generates real-time precise orbit and clock products using JAXA's MADOCA real-time analysis module, *MGRTE* (Kawate et al. 2023).

In *Step 1*, the positioning subsystem uses this real-time orbit and clock stream together with 1-Hz GEONET observations and performs PPP using RTKLIB's *rtkrcv*. PPP is performed using dual-frequency ionosphere-free combinations of GPS (L1/L2) and GLONASS (G1/G2) observations. Satellite antenna phase center corrections were applied using the IGS20 ANTEX file, and receiver antenna phase center corrections were applied using the GSI ANTEX file optimized for GEONET stations. Zenith total tropospheric delays were estimated as stochastic parameters without estimating horizontal gradients, using the Niell Mapping Function (Niel 1996) with the Saastamoinen a priori model (Saastamoinen 1972). Solid Earth tides, ocean tidal loading, and pole tides were corrected. An elevation cutoff angle of 15° was applied to exclude low-elevation observations.

A key difference from RTK processing is that RTK uses external ultra-rapid products (e.g., from CODE (CODE, 2026)) as input, whereas PPP is driven by the real-time orbit and clock products generated in-house using the IGS Real-Time Service stations (IGS 2026). This design reduces dependence on any single analysis center's product and improves system robustness. *Steps 2* and *3* then follow the same workflow as in the RTK clusters.

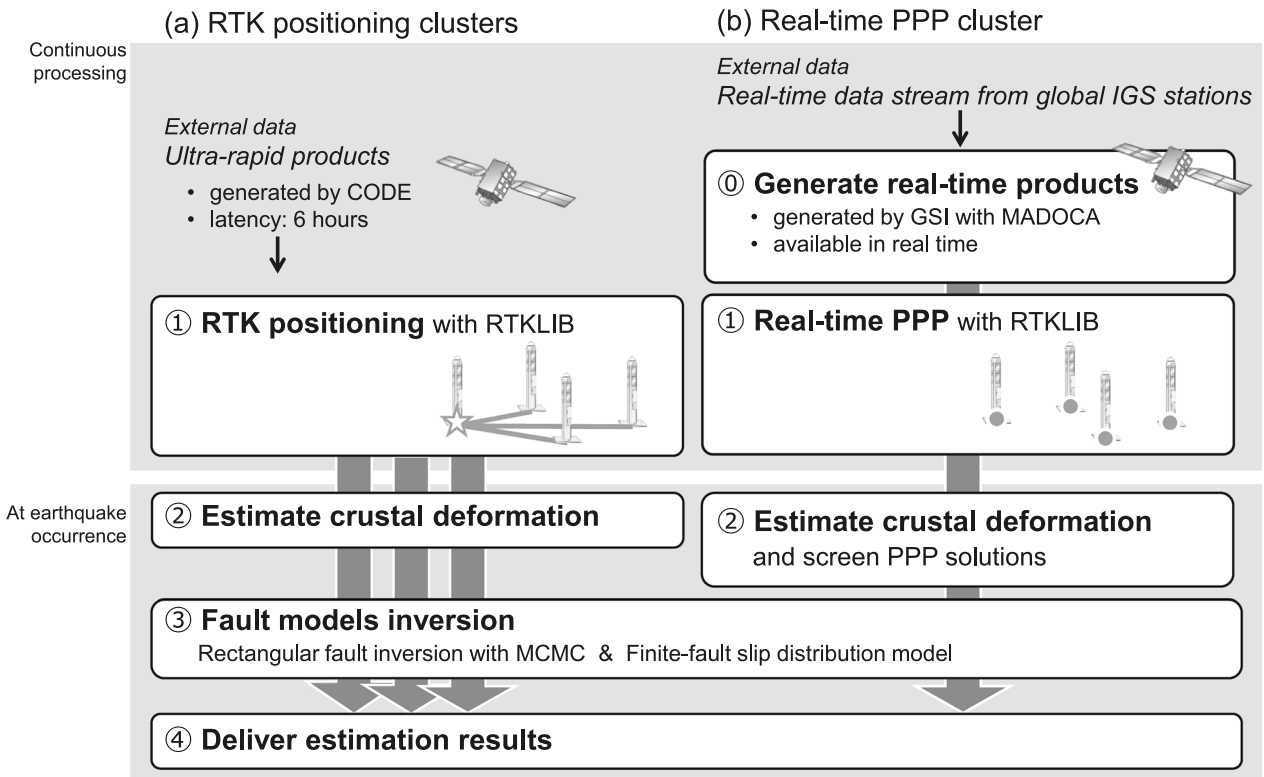


Fig. 1 REGARD processing workflow: **a** RTK clusters; **b** real-time PPP cluster

The following sections describe two additional data-screening procedures applied only to *Step 2* of the PPP cluster (the crustal-deformation calculation subsystem), which are intended to reduce systematic residual correlations that would otherwise bias probabilistic inference.

2.2.1 Large-noise removal

In the PPP cluster, the crustal-deformation calculation subsystem automatically excludes stations based on the per-epoch formal error output by RTKLIB's PPP solution. Specifically, for each station we compute the maximum 3D formal error within the 40 s time window used to estimate coseismic displacement (20 s before and 20 s after the earthquake; Kawamoto et al. 2017). If this maximum exceeds 0.14 m, the station is excluded from the inversion. The threshold was determined from 2 months of statistics across all stations to ensure that the screening is effective without being overly aggressive (Fig. S3). This procedure prevents stations affected by localized environmental noise and exhibiting unstable behavior during the reinitialization period from contaminating the fault-model estimation.

Figure 2a shows an example. Approximately 5 min before the earthquake, a data gap triggered a reset of the PPP Kalman filter, producing an erroneously large apparent displacement (>40 cm). The proposed screening successfully identified and removed this station.

2.2.2 Trend reduction

Because PPP performance depends on the accuracy of real-time orbit and clock products, network-wide position fluctuations of several centimeters may occur. This common-mode behavior arises, because the satellite orbit and clock errors act as shared inputs across all stations, causing their effects to propagate throughout the entire network. Trial operations of REGARD showed that this noise can exhibit stronger spatial coherence than the translational noise observed in RTK solutions and can, therefore, be removed effectively. To reduce these common-mode trends, we estimate a network-wide trend using stations sufficiently far from the epicenter—where coseismic deformation is expected to be negligible—as follows:

i. Stations are first sorted by epicentral distance, and the mean displacement for each component (X, Y, and Z) is computed using stations within the xth–95th percentile of the distance distribution. Here, x=20 when M_{eew} is below 6.5, and x=70 otherwise.

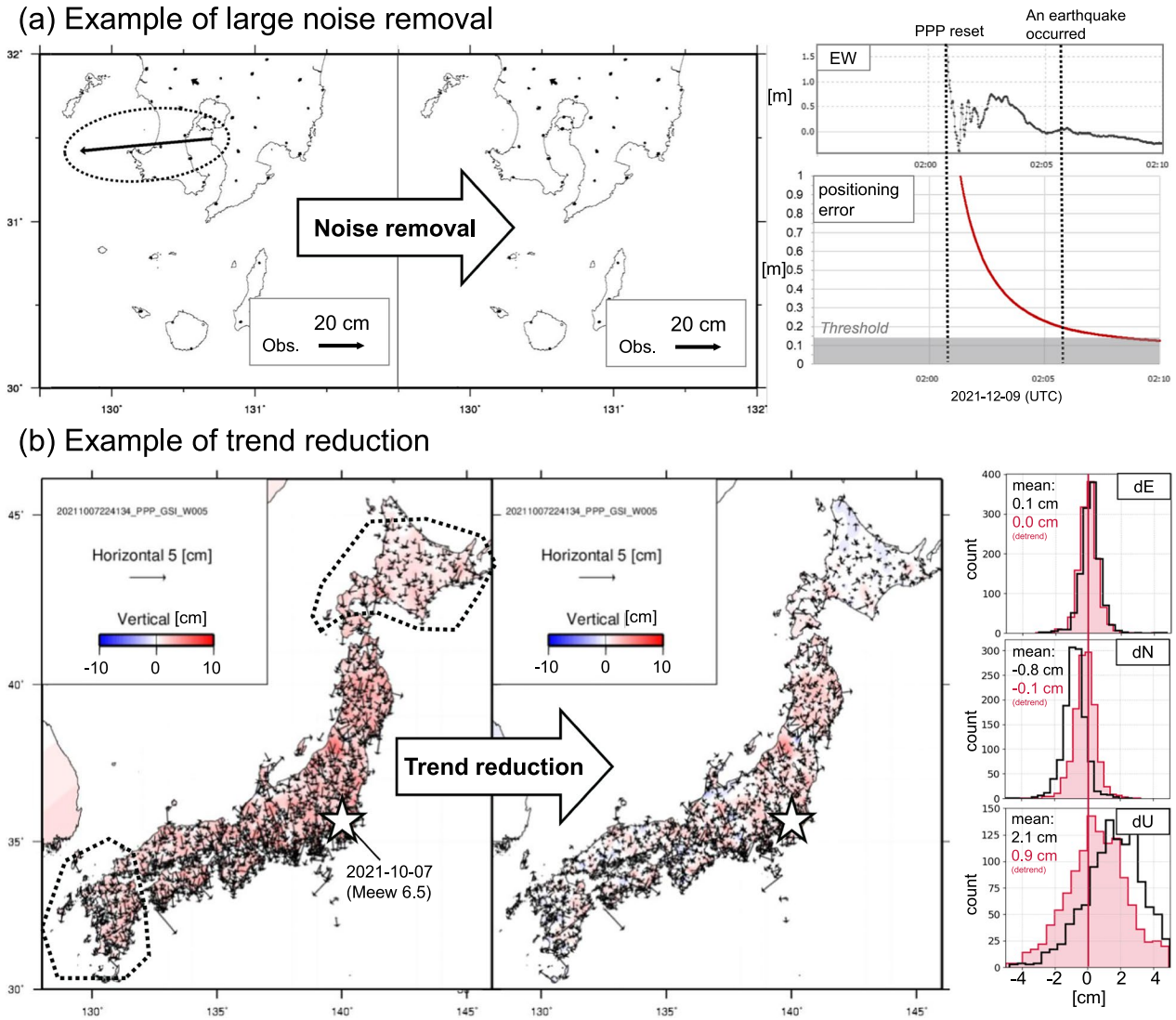


Fig. 2 **a** Example of a large spurious displacement at a single station in real-time PPP. A PPP reset occurred ~ 5 min before the earthquake, and the reinitialization temporarily increased positioning errors. **b** Example of trend removal. Map: orange stations (70th–95th percentile in epicentral distance) are used to estimate the trend. Histogram: red indicates the distribution after trend removal; the shape is preserved, while the mean shifts toward zero

ii. The estimated trend is then subtracted from the displacement vectors of all stations.

The percentile thresholds were selected to ensure that the stations used for trend estimation are located outside the expected deformation zone, based on empirical scaling relationships between earthquake magnitude and rupture extent. Sensitivity tests indicate that moderate variations in these percentile ranges do not change the inferred Mw beyond its estimated uncertainty bounds. Figure 2b shows an example of an event with $M_{eew} \geq 6.5$ in the Kanto region. In this case, the trend estimated from the 70th–95th percentile distance range was removed from all stations, reducing spurious common-mode error in the displacement field, as confirmed by both the map view and the histogram.

Through these implementations, the introduction of PPP fundamentally removes the structural limitations inherent in RTK positioning that arise from reference-station dependence, while the newly implemented screening and detrending procedures mitigate PPP-specific instabilities. As a result, improvements in positioning stability enhance the overall robustness of the system.

3 Results

3.1 Performance of MCMC

The MCMC-based rectangular fault estimation method implemented in RUNE entered trial operation in 2021 and was integrated into REGARD in 2025, fully replacing the previous MLE-based inversion. In this section, we evaluate its performance using real-time solutions for the 2024 Noto Peninsula earthquake, the 2024 Hyuganada earthquake, and the 2025 Aomori–Oki earthquake, together with summary statistics accumulated over approximately 5 years of trial operation. All results reported here were generated automatically within 10 min of earthquake detection.

3.1.1 2024 Noto Peninsula earthquake

The 2024 Noto Peninsula earthquake (M7.6) occurred on 1 January 2024 at 07:10 UTC as an inland reverse-fault event. REGARD successfully delivered both MLE-based and MCMC-based rectangular fault estimates to the relevant agencies.

Real-time RTK time series at stations that recorded large displacements are shown as blue curves in Fig. 3a–c. At station *0053*, a temporary data outage occurred after the strong shaking subsided due to communication disruption; however, the station soon recovered and ultimately recorded approximately 1.3 m of horizontal displacement, representing the largest deformation captured by REGARD during this event (Fig. 3a). In contrast, station *P111* stopped transmitting immediately after the earthquake due to physical damage (Fig. 3c). Several additional nearby stations also experienced intermittent outages (Fig. 3d).

Despite the absence of near-epicentral data, the system captured the regional deformation pattern, enabling both RUNE and the MLE procedure to successfully estimate rectangular fault models. Figure 4 shows the RUNE

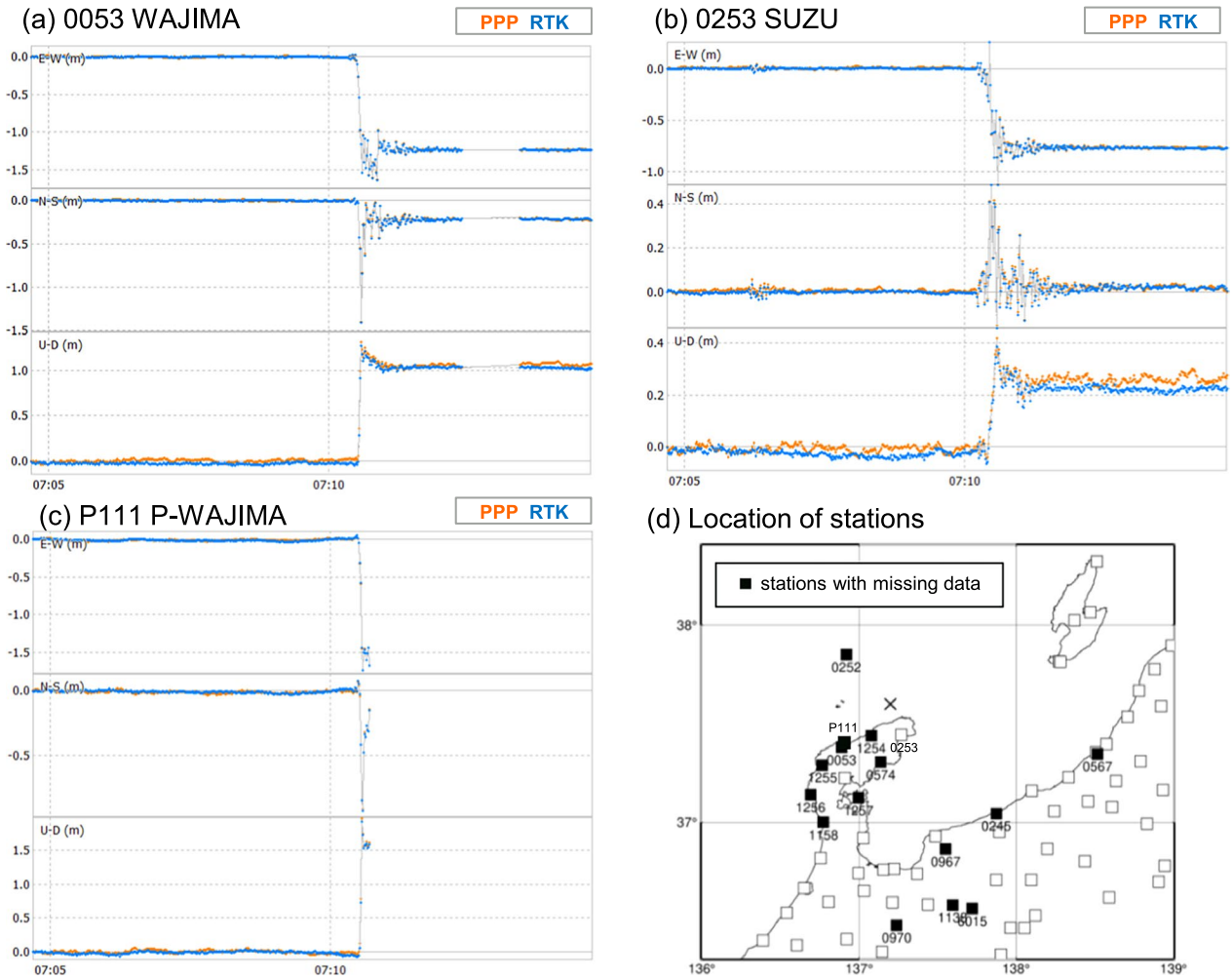
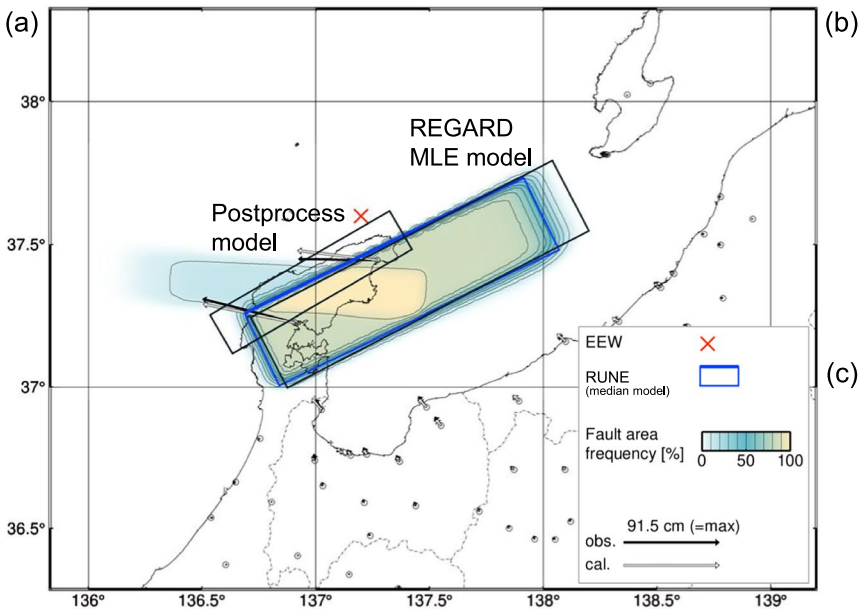


Fig. 3 **a**–**c** Real-time RTK time series at stations *0053*, *0253*, and *P111*, using *KITAHATA* as the reference station. **d** Locations of stations with missing data



		median	min.	max.
Mw		7.44	7.36	7.67
VR	[%]	93.62	81.61	94.01
lat.	[deg]	37.37	37.29	37.43
lon.	[degl	137.38	136.69	137.51
depth	[km]	5.41	1.51	17.32
strike	[deg]	64.06	57.69	281.19
dip	[deg]	6.00	0.00	15.04
rake	[deg]	135.43	-46.61	146.68
length	[km]	120.86	78.58	145.81
width	[km]	31.54	12.40	41.03
slip	[m]	1.59	1.27	8.32

Fig. 4 RUNE results for the 2024 Noto Peninsula earthquake. **a** Estimated fault model (median). Black and white vectors represent observed and modeled displacements, respectively. Contours indicate the normalized frequency of sampled fault planes. Black rectangles show the REGARD MLE model and a post-processed model estimated using RUNE with post-event recovered R5 coordinates. **b** Fault parameters. **c** Probability distribution of Mw

results at 07:14:46 UTC (276 s after detection), together with the REGARD MLE solution. The fault parameters estimated in real time by RUNE and MLE converged to similar values in terms of the magnitude and fault geometry, and no major differences in parameter estimates attributable to the estimation method were observed in this case (Fig. 4a; Table S1). Although these REGARD models are constrained by the absence of near-field observations and the assumption of a single-rectangular fault, RUNE yielded a moment magnitude of Mw = 7.44 with quantified uncertainty (Fig. 4b, c; other parameters in Fig. S4), assuming a rigidity of 30 GPa. This magnitude is consistent with a post-processed model derived from recovered data (Mw = 7.40, rigidity = 30 GPa), obtained by re-estimating the fault-model offline using GNSS observations that were unavailable in real time due to communication outages (e.g., Fig. 3d) but later retrieved (GSI 2024a). Using these recovered observations, we re-estimated the fault model with RUNE under the same framework, and the resulting magnitude is also consistent with both the real-time estimates and the GSI (2024a) solution (Mw = 7.44, rigidity = 30 GPa).

In contrast, the real-time fault geometries differ from the post-processed models. In particular, the dip angle shows a significant difference: real-time RUNE estimated a low-dip angle of 6.0°, whereas GSI (2024a) reported a dip range of 40.6°–54.9°. In addition, Yamada et al. (2025) demonstrated through a grid-search validation of fault dip angles, that a high-angle dip model is required to adequately explain the nearby vertical displacement components. This discrepancy is not primarily controlled by the prior, because, as described in Sect. 2.1, the dip angle is not subject to a strongly informative prior constraint, whereas the strike is derived from the bimodal prior distribution. Although the dip angle was initially set to 45° in this case, it was allowed to vary under a uniform prior PDF, and the convergence point was determined by data constraints. This reflects a design choice to avoid overly constraining parameters that influence characteristics of tsunami sources. In Fig. 4b, the uncertainty bounds show the full posterior range (minimum–maximum) of the MCMC samples, and even across this entire range the dip angle remains shallow, indicating that the real-time data—not the limits of the exploration domain—systematically favor a low-dip solution. Given that the post-processed model using recovered data (Fig. 4a) yielded a dip of 36.2°, this discrepancy likely reflects both the absence of near-field observations in real time and the inherent limitation of approximating a complex rupture geometry with a single-rectangular fault. In such cases, the likelihood provides insufficient constraints on dip, allowing solutions that are compatible with sparse observations but differ from those obtained with more complete datasets. The impact of missing data is discussed further in Sect. 4.3.

3.1.2 2024 Hyuga-nada earthquake

The 2024 Hyuga-nada earthquake (M7.1) occurred on 8 August 2024 at 07:42 UTC. REGARD operated normally, and the MLE-based solution, which was used operationally as the primary product at the time, was submitted to the Nankai Trough Earthquake Assessment Committee, which discusses the likelihood of a large earthquake in the Nankai Trough and issues Nankai Trough Earthquake Extra Information to the public (JMA 2026).

Figure 5 shows the RUNE results at 07:44:05 UTC (62 s after detection). The estimated model is consistent with both the MLE and post-processed (GSI 2024b) fault

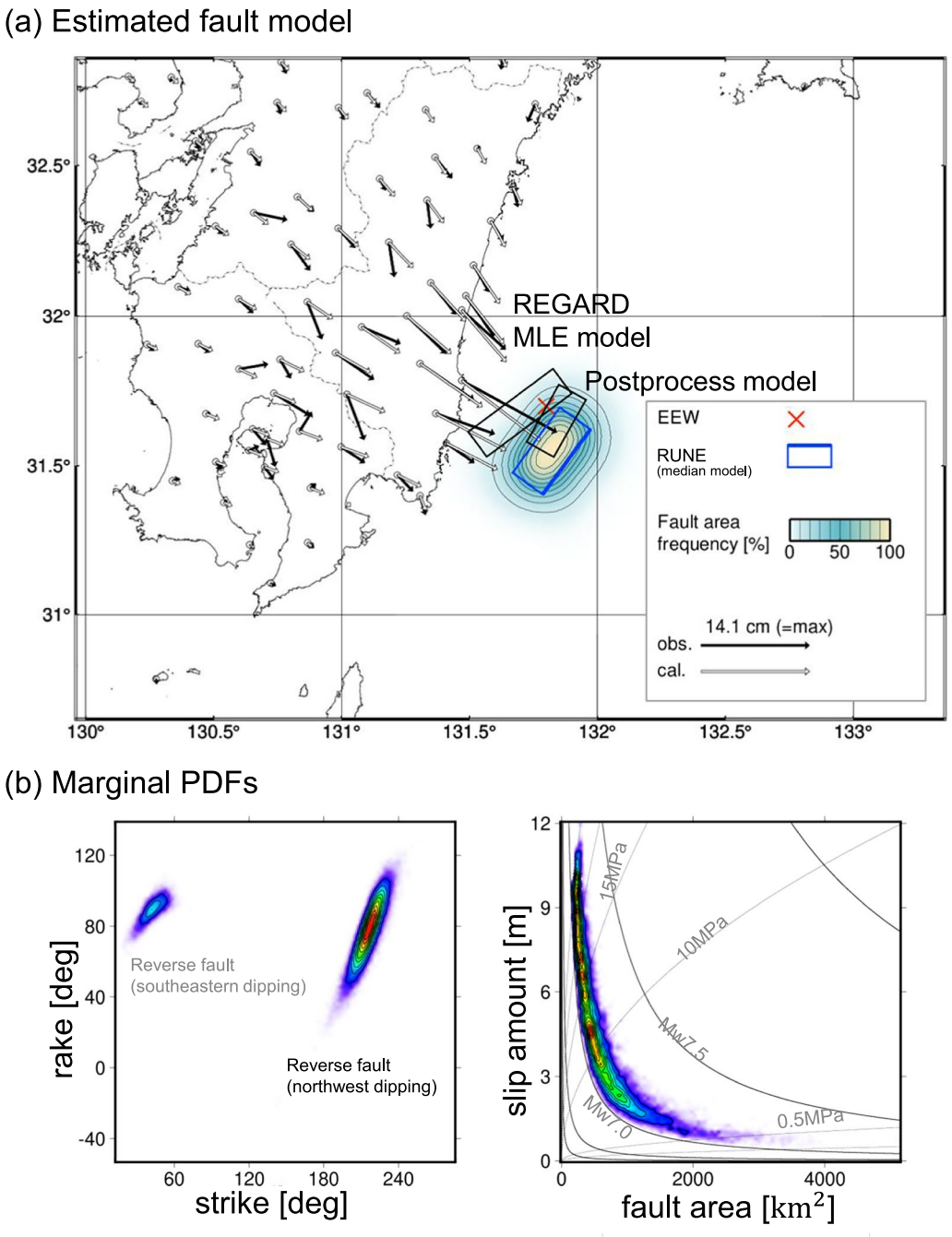


Fig. 5 RUNE estimation results for the 2024 Hyuga-nada earthquake. **a** Estimated fault model (median). Black and white vectors represent observed and modeled displacements, respectively. Contours indicate the normalized frequency of sampled fault planes. Black rectangles show the REGARD MLE model and the post-processed model (GSI 2024b). **b** Marginal posterior probability distributions

models (Table S2). RUNE estimated Mw = 7.15 assuming a rigidity of 30 GPa, which is close to the post-processed estimate of Mw = 7.10 (reported using a rigidity of 60 GPa).

The marginal posterior distributions of strike and rake exhibit two distinct clusters (Fig. 5b; each PDF in Fig. S5), indicating a dominant northwest-dipping fault and a possible southeast-dipping conjugate plane. In addition, a clear trade-off between fault area and slip is observed along contours of constant Mw. These marginal PDFs are available to internal operators, enabling rapid interpretation of uncertainty in offshore source estimation based on land-based GNSS data. Quantifying uncertainty in real time also allows the reliability of a single representative solution to be evaluated more objectively.

3.1.3 Statistical evaluation of operational performance

After approximately 5 years of trial operation, RUNE was formally adopted as the primary inversion method in July 2025, replacing the MLE-based approach. Figure 6a shows the frequency distributions of VR for both MLE and RUNE derived from operational data. The RUNE distribution exhibits a pronounced peak near VR ≈ 0, indicating that the method tends not to fit noise-dominated displacement fields. In contrast, the MLE approach frequently yields high VR values even in noise-dominated cases, leading to false alarms. While VR is commonly used as a measure of goodness of fit, it can be artificially high in noise-dominated cases, leading to overfitting rather than improved model performance. RUNE suppresses such behavior and produces low VR values when no significant deformation is present, indicating that noise fitting is effectively avoided. Consistent with this interpretation, the proportion of false alarms—defined as cases with VR ≥ 80% despite the absence of significant deformation—decreased from 2.091% with MLE to 0.001% with RUNE, based on 3,731 trigger samples. These results demonstrate that uncertainty-aware inversion not only provides probabilistic information but also structurally improves robustness by preventing noise-driven overfitting.

Figure 6b compares the Mw estimates obtained using MLE and RUNE with the EEW magnitude, M_{eew}. For events with confirmed significant deformation (red points), the RUNE estimates generally agree with the MLE results, with their uncertainty intervals overlapping in most cases. For these events, both the MLE- and MCMC-based Mw estimates tend to be closer to the JMA magnitude (Fig. 6b, inset) than to M_{eew}. In contrast, an apparent Mw–M_{eew} correlation emerges in noise-dominated cases. Importantly, this trend reflects not genuine crustal-deformation signals but the scaling law

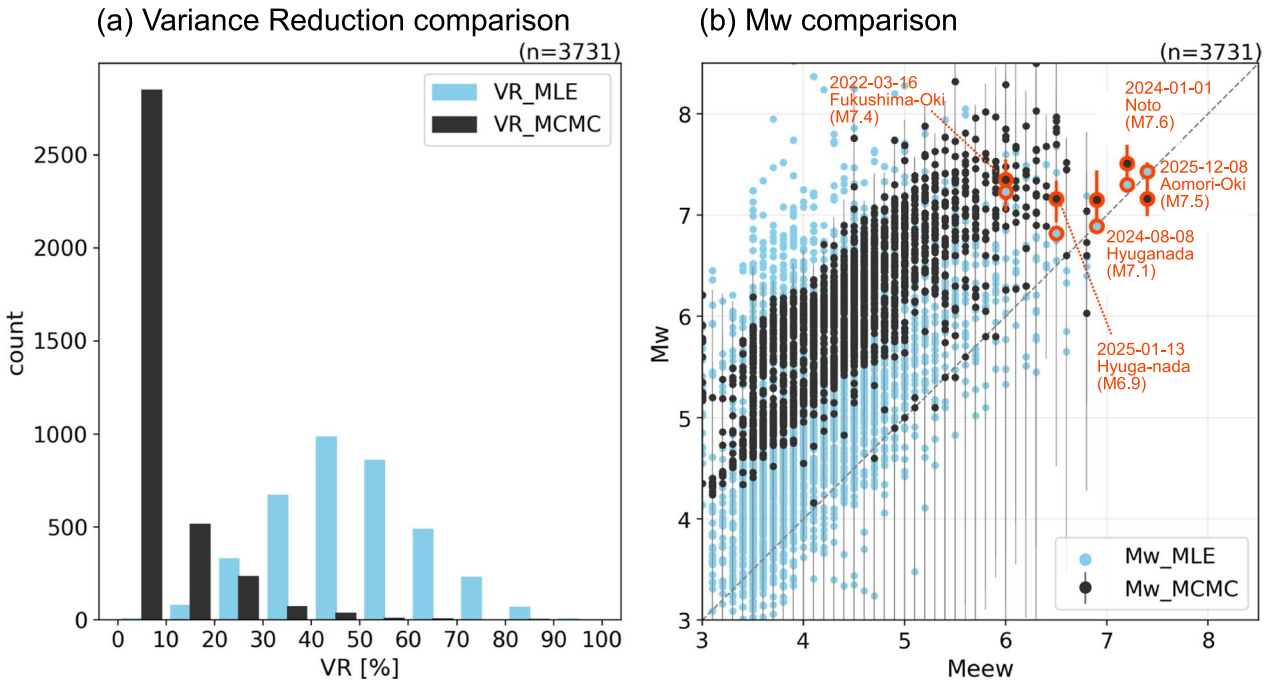


Fig. 6 **a** Frequency distributions of variance reduction (VR) for 3731 event samples with M_{eew}3 or greater from 2022 to 2025. Filled symbols: maximum-likelihood estimation (MLE); open symbols: Markov chain Monte Carlo (MCMC). **b** Comparison of moment magnitude (Mw) estimated by MLE and MCMC with the M_{eew}. Skyblue symbols: MLE; black symbols: MCMC. For each event, the MLE and MCMC estimates share the same horizontal coordinate. Red annotations highlight deformation-observed events, with labels indicating the event date, region, and JMA magnitude

based on M_{eew} used for the initial values of fault length and width in RUNE. Moreover, when noise dominates the observations, RUNE tends to produce Mw values larger than M_{eew}. This tendency arises from the prior design for the parameters controlling seismic moment: fault length and width are assigned normal-type priors derived from scaling relations, whereas slip is given a non-informative prior (i.e., without magnitude-dependent constraints) (Ohno et al. 2021). This choice maintains flexibility for unanticipated scenarios; however, when the likelihood is weak, it can lead to an overestimation of Mw, because the representative value is computed from the median of broadly sampled slip values. This tendency is not observed in high-signal-to-noise events (Fig. 6b), which are the primary focus of REGARD, as the likelihood dominates the posterior. In addition, in the MCMC framework, the VR exhibits larger sensitivity to S/N than MLE (Fig. 6a) and provides a more robust indicator for solution reliability. Therefore, this does not negatively affect operational use.

The 2025 Aomori–Oki earthquake (M7.5) was the first M7-class event after the full adoption of RUNE, and the real-time output formats are shown in Fig. 7. RUNE estimated Mw = 7.51, consistent with post-processed results (e.g., GSI 2025). The representative median model differed from the post-processed model by approximately 90° in strike, corresponding to the conjugate plane. The posterior distribution (Fig. 7) is bimodal in strike and rake; although the median corresponds to the higher-probability mode, the alternative plane consistent with the post-processed model was also explored. This likely reflects the limited resolving power of real-time GEONET data for offshore sources, particularly because north–south constraints are weaker. Even when the representative median model differs from post-processed solutions, the system explicitly indicates what can and cannot be resolved in real time, providing uncertainty information that is essential for operational decision-making.

3.2 Performance of real-time PPP

Real-time PPP began trial operation in 2023 as a new analysis cluster and was incorporated into REGARD in 2026. Below, we demonstrate the improvements and remaining challenges by comparing the PPP results with those obtained from RTK.

3.2.1 Resolving RTK positioning challenges

The advantages of PPP become most apparent not during clear coseismic events but under noise-dominated conditions. Because PPP processes each station independently, anomalies originating at a single station do not propagate coherently across the network, unlike in RTK. When displacement is evaluated over REGARD's operational time window (~5 min), the steady-state noise level of real-time PPP is comparable to that of RTK (Fig. 8a). Moreover, during periods when RTK exhibits pronounced nationwide translational noise, PPP effectively suppresses the corresponding network-wide bias when applied to the same time intervals (Fig. 8b).

By eliminating RTK translational noise, PPP more closely satisfies the near-zero-mean residual assumption of the inversion. This effect complements the σ-floor constraint that prevents data overfitting, together forming a two-tiered safeguard against noise-driven overfitting and thereby enhancing overall operational robustness.

3.2.2 2011 Tohoku–Oki earthquake

Although real-time PPP was not applied at the time of the 2011 Tohoku–Oki earthquake, we post-processed PPP analysis to evaluate its performance during a major event. Figure 9a compares displacement time series at *0550*, where very large displacements were observed. The RTK baseline solution relative to *0001* (*WAKKANAI*; Northernmost part of the Hokkaido region) is shown in blue, whereas the PPP solution for *0550* alone is shown in orange. PPP reproduces the coseismic displacement with accuracy comparable to that of RTK. Even in the presence of such large signals, formal errors remained small, indicating that the screening procedure described in Sect. 2.2 is unlikely to erroneously exclude stations experiencing genuine deformation.

A closer inspection of the time series (Fig. 9a, upper right) reveals oscillations of approximately 5 cm that appear only in the RTK baseline solution. When the PPP time series at *0001* is subtracted from that at *0550*, these short-period fluctuations are accurately reproduced (Fig. 9a, lower right). This confirms that the oscillations are caused by the passage of surface waves (Furumura

(See figure on next page.)

Fig. 7 Estimation results for the 2025 Aomori–Oki earthquake (Real-time output format within 10 min of the earthquake). **a** Map view. The blue line shows the model with median values of posterior probability density functions (PDFs). The contours indicate normalized uncertainties in the spatial model area. The black and white vectors indicate the observed and calculated values, respectively. **b** Posterior PDFs. The ranges on the horizontal axis reflect the maximum search ranges. Inserted values in the upper right-hand corner denote the median, mean, mode, 95% confidence interval, minimum value, and maximum value, respectively. The yellow dot lines and inserted texts in the bottom-right indicate prior PDFs

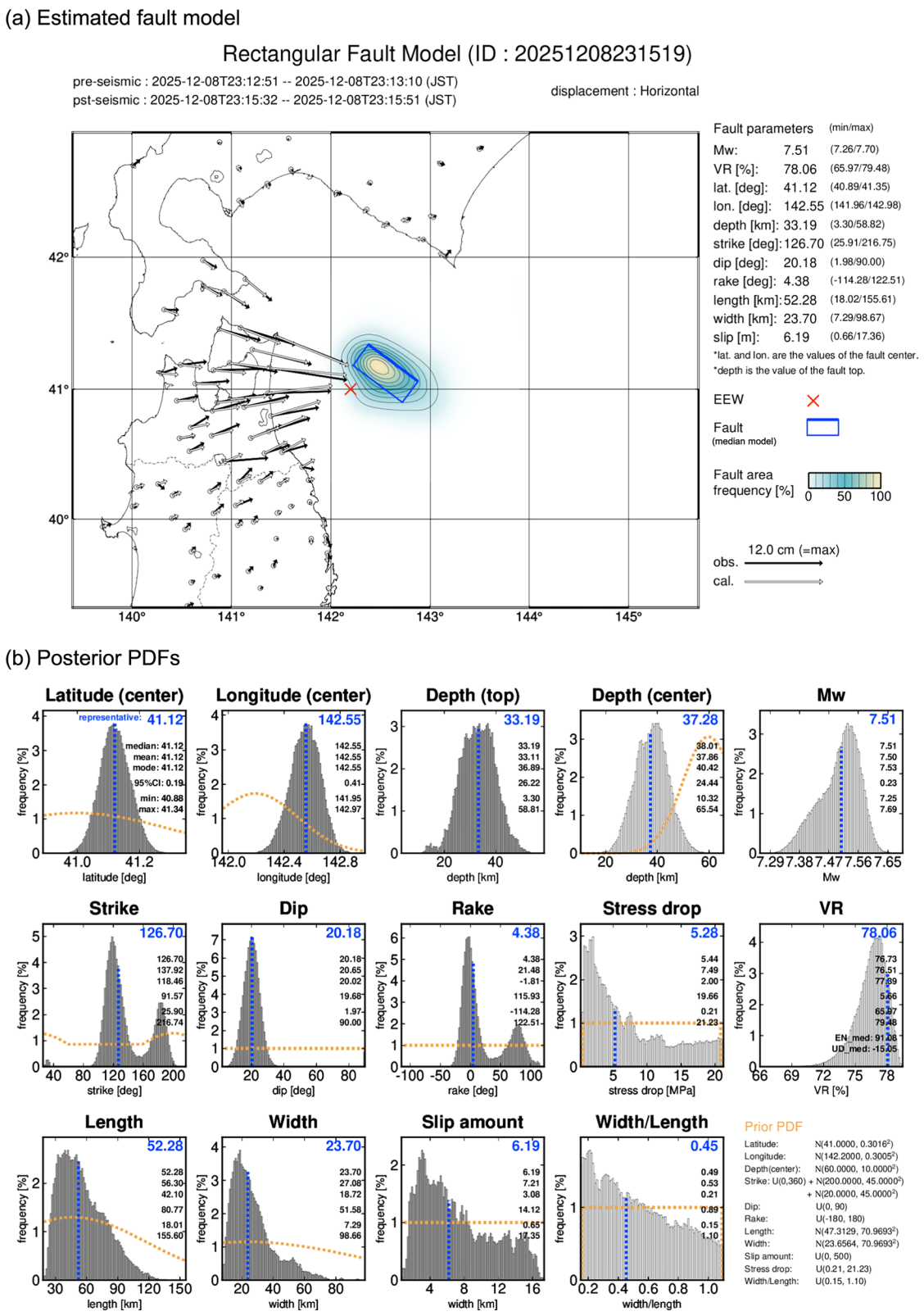


Fig. 7 (See legend on previous page.)

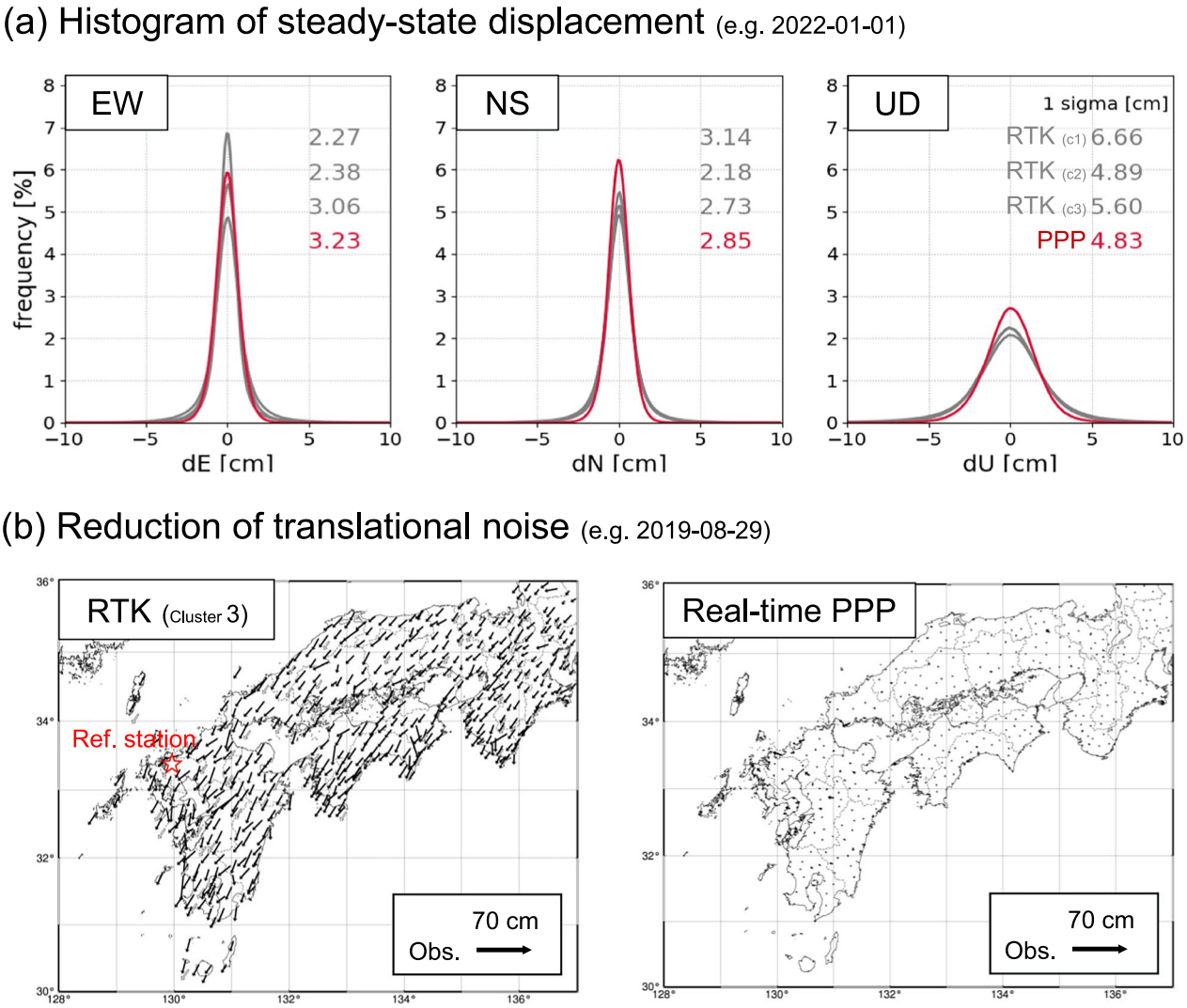


Fig. 8 Evaluation of steady-state noise levels in real-time PPP. The real-time PPP results are obtained after applying outlier removal and trend-reduction processing. **a** Dispersion of displacement estimates. Gray denotes the three RTK clusters, and red denotes the real-time PPP cluster. Inserted values indicate standard deviations. **b** Example of PPP results during a period dominated by translational noise in RTK

2014) at the RTK reference station and demonstrates that PPP successfully eliminates reference-station dependence.

Using the PPP-derived displacement field, we estimated both a rectangular fault model and a slip distribution model (Fig. 9b, c) using the conventional MLE approach following Kawamoto et al. (2017) based on the data analyzed in this study. These results are shown to confirm that the PPP-derived displacements do not affect REGARD's model estimation. Because the primary difference between the PPP and RTK displacement fields is the small transient oscillation described above, the estimated fault models closely match those reported by Kawamoto et al. (2017).

3.2.3 Trial operational performance

The PPP cluster began trial operation in 2023. Here, we summarize its behavior during the 2024 Noto Peninsula and 2024 Hyuga-nada earthquakes. During both events, PPP operated as a fourth experimental cluster; at that time, PPP-based displacement calculation and fault inversion had not yet been implemented in real time. Therefore, the PPP outputs were post-processed using RUNE for evaluation.

For the 2024 Noto Peninsula earthquake, PPP captured the earthquake-related offsets and outages at *0053*, *0253*, and *P111* (Fig. 3a–c, orange curves) in a manner consistent with RTK. During this event, the centimeter-scale, network-wide PPP noise described in Sect. 2.2

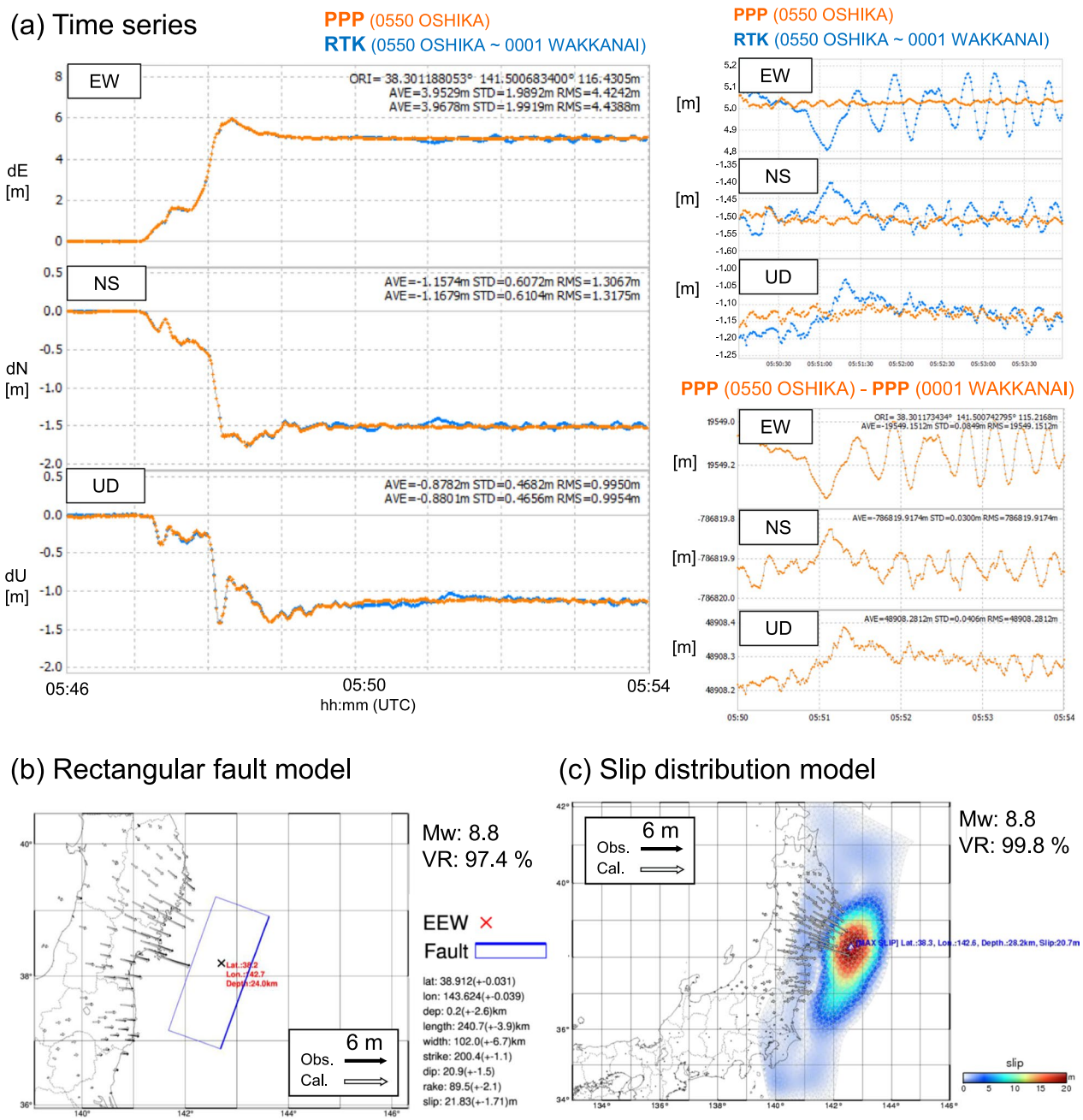


Fig. 9 **a** Time series at GEONET station *0550* during the 2011 Tohoku–Oki earthquake, comparing real-time PPP and RTK. Right: zoomed-in view of the later time window. Bottom: difference between the PPP time series at *0550* and *0001*. **b** Estimated rectangular fault model using PPP-derived displacements with MLE. **c** Estimated slip distribution

was also observed (Fig. S6). Residual analysis revealed a southwestward horizontal trend of ~ 2 cm and a vertical uplift bias of several centimeters in the PPP solutions. After applying the trend-reduction procedure, the PPP-derived displacement field became more consistent with the RTK-based pattern, indicating that the treatment of network-wide translational trends can directly affect inversion outcomes (Fig. S6). Such trends cannot be automatically absorbed by RUNE's likelihood function, which assumes zero-mean residuals, underscoring the importance of the trend-reduction step.

For the 2024 Hyuga-nada earthquake, station *0483* recorded permanent displacements on the order of centimeters. The PPP solution was more stable than the RTK

solution in the horizontal components, whereas the vertical component exhibited slightly larger scatter (Fig. S7). Rectangular fault models derived from PPP differed from the RTK-based solution mainly in strike, with VR values of 31% for PPP and 53% for RTK, while the estimated Mw values remained similar. The overall displacement field contained many low-signal-to-noise stations and lacked several coastal stations, weakening constraints on strike and making the inferred source appear more point-source-like, as is typical for offshore events. In this case, station exclusion influenced the model estimation, underscoring the need for additional conditioning and quality control of real-time PPP products.

For the 2025 Aomori–Oki earthquake, real-time PPP did not produce positioning results because the generation of real-time orbit and clock products halted due to an operational error.

4 Discussion

4.1 Utilizing uncertainty quantified by MCMC

The proposed MCMC framework demonstrates that uncertainty-aware inversion can function as a stabilizing mechanism in automated real-time systems, rather than merely providing supplementary diagnostic information. Here, we discuss how the quantified uncertainty can be interpreted and utilized.

Uncertainty information allows users to objectively assess the risk of under- or overestimation in the immediate aftermath of an event, thereby improving the reliability of rapid analyses. At the same time, uncertainty derived from MCMC sampling is inherently richer than conventional point estimates. Although presenting multiple plausible solutions and alternative models can benefit decision makers, overly complex output may hinder decision-making under time pressure. In operational practice, we, therefore, categorize outputs into indicators communicated succinctly to end users and indicators intended for internal use. This approach balances accuracy, speed, and brevity according to the needs of different users (e.g., JMA, the Cabinet Office, and railway operators).

Beyond visualization, uncertainty can also be propagated into downstream hazard-assessment systems to quantify secondary risks. Ohno et al. (2022) demonstrated an approach in which uncertainty in coseismic slip distributions is propagated through multiple samples into tsunami inundation simulations to quantify uncertainty in tsunami hazards. In this sense, MCMC-based uncertainty is not merely ancillary metadata but structural information that can enhance real-time disaster-mitigation systems.

In the remainder of this section, we examine the validity of the quantified uncertainty. Its magnitude depends on how aleatory uncertainty (e.g., observational errors; Hennig et al. 2015) and epistemic uncertainty (e.g., model errors; Kiureghian and Ditlevsen 2009) are represented. The system is designed to balance physically grounded constraints with sufficient inclusiveness to accommodate worst-case scenarios relevant to disaster mitigation.

4.1.1 Observational errors

Numerical experiments indicate that the automatically adjusted standard deviation of the Gaussian likelihood is consistent with the injected Gaussian noise (Ohno et al. 2021), suggesting that the method yields appropriate uncertainty estimates when residuals are approximately Gaussian. In the current implementation, RUNE adopts a normal likelihood (Ohno et al. 2021, 2024a). Because non-Gaussian noise (e.g., large station-specific noise or network-wide translational artifacts) is difficult to accommodate during real-time estimation, it is essential to suppress such effects at the observation or positioning stage. Although non-Gaussian residuals may still occur, reducing systematic components in the positioning process improves the validity of the Gaussian-residual approximation. Future extensions may incorporate heavy-tailed likelihood models.

4.1.2 Modeling errors and priors

RUNE's automatic adjustment determines σ based on residuals arising from the single-rectangular-fault approximation (Dettmer et al. 2014; Ohno et al. 2021). Consequently, greater model mismatch in a coarse representation leads to a larger σ, which helps maintain probabilistic validity. Furthermore, the lower bound introduced in Sect. 2.1 prevents unrealistically small σ values and avoids overfitting. In practice, we confirmed that σ often reaches the predefined lower bound in cases dominated by near-Gaussian white noise or very small displacements close to the noise level. In contrast, σ exceeds the lower bound when the data include outliers or when large coseismic displacements are present. This behavior indicates that the lower bound acts primarily as a safeguard in noise-dominated cases and does not significantly affect the results when signal amplitudes are large.

For epistemic uncertainty represented by prior distributions, we adopt a strategy of incorporating observational and physical prior information—such as EEW constraints and scaling laws—with sufficient strength to enhance stability in automated estimation.

4.2 Real-time PPP stability

The real-time PPP implementation introduced in this study substantially mitigates structural limitations inherent in RTK, specifically its dependence on a fixed reference station and its susceptibility to large-scale, network-wide translational noise, thereby

strengthening the positioning foundation of REGARD. At the same time, several aspects of real-time PPP still require improvement.

Real-time PPP critically depends on the continuity and stability of upstream precise products, particularly orbit and clock streams. If the real-time orbit or clock stream is interrupted, PPP processing halts immediately; therefore, reliable operation requires the continuous (24/7) generation and delivery of these precise products. During the Aomori-offshore event, positioning failed, because the real-time orbit stream was unavailable due to maintenance, which prevented the accumulation of case data. Although four redundant precise orbit and clock estimation subsystems are currently in operation, REGARD relied on a single stream at that time. Establishing a higher-level redundancy layer that monitors stream quality and automatically switches to the best available stream is, therefore, essential.

With respect to positioning quality, the proposed screening procedures effectively address two major challenges: large station-specific noise and system-wide translational noise. That said, for station-specific anomalies, the current strategy relies on excluding the affected stations, which can degrade model estimation (Sect. 3.2.2). Because REGARD routinely processes observations from nearly 1,300 GNSS stations, data gaps and intermittent outages are unavoidable in practice. In the next section, we therefore examine how missing observations affect the inversion and discuss strategies to suppress noise-driven overfitting under conditions of data loss.

4.3 Addressing position instability in model inversion

In real-time GNSS analyses, simultaneous data gaps may occur immediately after an earthquake due to station damage, communication outages, equipment malfunctions, or processing failures. During the 2024 Noto Peninsula earthquake, two stations ceased operation because of physical damage, and additional outages occurred due to communication disruptions (Fig. 3c). As a result, the inversion overfit the remaining observations and produced an unrealistically shallow-dipping fault model (Fig. 4). Such underestimation of the dip angle could lead to underestimation of tsunami inundation in downstream applications. In addition, PPP instability during the trial-operation stage can itself introduce data gaps (Sect. 4.2). Although these issues should ultimately be mitigated through improvements to the positioning subsystem, here we focus on their impact on MCMC-based fault estimation and describe the countermeasures implemented in RUNE.

RUNE performs the inversion using only stations for which displacements can be successfully computed. Consequently, data gaps effectively alter the spatial coverage of the observation network and may bias the inferred model.

4.3.1 *Missing-data detection*

REGARD uses approximately 200 GNSS stations as displacement inputs, including 50 stations located near the epicenter and about 150 additional stations selected through distance-based down sampling. For the 50 near-field stations, a predefined template list is compared with the set of stations for which displacement estimates are available; any discrepancy between the two sets is treated as missing data.

4.3.2 *"Missing-data mode" to suppress overfitting*

To reduce noise-driven overfitting under conditions of data loss, we introduce a *missing-data mode* in which the likelihood standard deviation (σ) is inflated in proportion to the observed displacement amplitude. Specifically, among the ten stations closest to the epicenter, we compute, for each station, the second-largest absolute displacement across the three components and denote the resulting representative amplitudes as d_E, d_N, and d_U. We then define the minimum value of σ as

$$\sigma_{EN} = 0.1\sqrt{d_E^2 + d_N^2}, \sigma_U = 0.1|d_U| \tag{5}$$

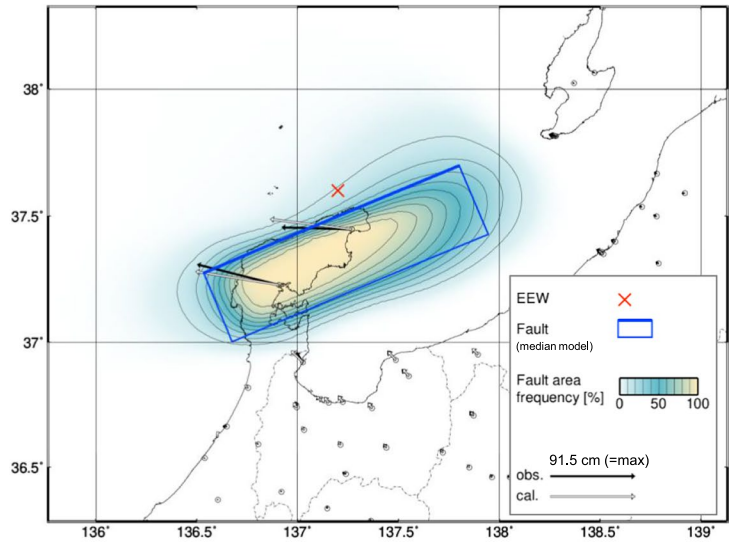
We adopt the larger of this σ and the value of σ determined automatically in the normal mode. In addition, if $\sigma_U < \sigma_{EN}$, we set $\sigma_U = \sigma_{EN}$ to avoid imposing overly restrictive constraints on the vertical component. The 10% scaling factor was selected based on retrospective tests using the 2024 Noto Peninsula earthquake: larger factors tended to underestimate Mw, whereas smaller factors failed to prevent unrealistically shallow-dip estimates. Using the second-largest displacement reduces sensitivity to isolated outliers.

Applying the missing-data mode to the 2024 Noto Peninsula earthquake (Fig. 10a) broadens the feasible parameter region relative to Fig. 4. Although the median model remains broadly consistent, the posterior range expands; notably, the upper bound of the dip angle increases from 15° to 52°, mitigating the previously observed shallow-dip bias. Even in missing-data mode, the median estimate generally converges with a model similar to that obtained under normal operating conditions.

4.3.3 *Using expanded uncertainty to extract a practical worst-case model*

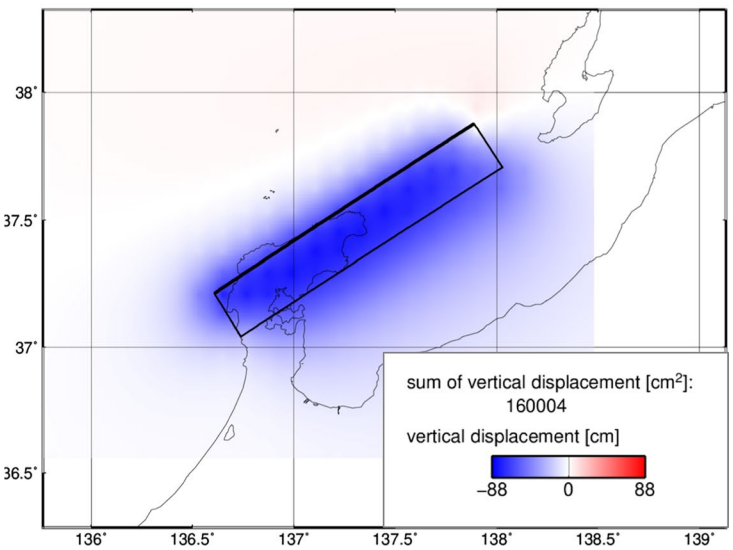
To make practical use of the expanded uncertainty, downstream use of multiple samples becomes important. One possible approach is ensemble scenario simulation (Ohno et al. 2022), but such simulations can be

(a) Estimated result with data shortage mode



		median	min.	max.
Mw		7.45	7.09	8.62
VR	[%]	94.63	82.24	96.06
lat.	[deg]	37.35	37.11	37.95
lon.	[degl	137.24	136.39	137.61
depth	[km]	4.84	0.00	18.78
strike	[deg]	67.18	0.08	360.00
dip	[deg]	9.53	0.00	52.55
rake	[deg]	138.75	-107.58	179.73
length	[km]	121.84	48.25	256.50
width	[km]	33.21	9.56	152.46
slip	[m]	1.57	0.80	45.48

(b) Worst case extracted from samples in data shortage mode



		1 sample
Mw		7.44
lat.	[deg]	37.46
lon.	[degl	137.32
depth	[km]	6.91
strike	[deg]	56.98
dip	[deg]	14.33
rake	[deg]	115.54
length	[km]	135.62
width	[km]	23.37
slip	[m]	2.71

Fig. 10 **a** RUNE estimation results using the "missing-data mode." **b** Worst-case model extracted from the missing-data posterior. Colors indicate vertical displacement computed using Okada (1992) over the region explored in missing-data mode

computationally demanding in real time. As an alternative, we explore extracting a plausible worst-case model from the MCMC samples.

Ohno et al. (2022) reported a positive correlation between the sum of absolute vertical seafloor deformation and the resulting inundation area. Motivated by this relationship, we select a worst-case sample as follows:

i. Filter the MCMC samples according to the following criteria:

A) epicenter latitude and longitude within the 95% CI;
B) VR above the lower bound of the 95% CI;
C) stress drop within the 95% CI;
D) dip within the quartile bin that contains 45° (i.e., partitioning the range 0°–90° into Q1–median–Q3).

ii. Compute the vertical seafloor deformation for each retained sample using the formulation of Yoshimitsu Okada (1992).
iii. Select the sample that maximizes the summed squared vertical displacement.

Criterion (D) targets dip angles near 45°, based on the finding that tsunami height is relatively insensitive to dip (e.g., Baba et al. 2024) while still balancing uplift amplitude and spatial extent. Criteria (A)–(C) are intended to avoid selecting extreme outliers that are unrepresentative of the posterior distribution. For the spatial domain used to evaluate the initial deformation, we project all MCMC fault samples onto a map and define the latitude–longitude bounds that encompass the entire set of samples.

Although this worst-case selection procedure is independent of the missing-data mode, combining the two enables effective use of the expanded parameter space. Figure 10b shows the worst-case sample extracted from the posterior obtained in the missing-data mode. Compared with the median models in Figs. 4b and 10a, the worst-case solution exhibits larger slip and a steeper dip. Although full tsunami inundation simulations are beyond the scope of this study, the result suggests a practical pathway to reduce the risk that shallow-dip real-time models underestimate tsunami hazard when used as input for downstream applications.

Although PPP and MCMC cannot prevent data gaps, their combined use provides a mechanism to quantify the resulting reduction in model reliability when observations are missing. Together with ongoing improvements in observational infrastructure, further advances in inversion strategies and uncertainty quantification under missing-data conditions will help strengthen the robustness of real-time systems.

5 Conclusions

We implemented two major operational upgrades to REGARD: (i) a real-time MCMC inversion framework that provides quantitative uncertainty estimates and (ii) a real-time PPP positioning cluster that eliminates structural limitations inherent to RTK. Together, these upgrades address two long-standing challenges in real-time GNSS coseismic analysis: the lack of explicit uncertainty quantification and contamination by reference-station-dependent noise.

The MCMC framework estimates the posterior probability density functions (PDFs) of Mw and fault parameters within the operational time window. Prior constraints and a likelihood σ-floor suppress noise-driven overfitting while preserving sensitivity to genuine deformation, yielding uncertainty-aware fault estimates that reflect the resolving power of the available data. Real-time PPP stabilizes the observation layer by eliminating reference-station dependence and the associated translational artifacts. In addition, station screening and common-mode trend removal further improve the consistency of the displacement field and support the assumptions underlying the Bayesian likelihood.

Applications to recent earthquakes and long-term operational statistics show that the combined upgrades substantially reduce false alarms while maintaining consistency with post-processed solutions. Although uncertainty remains large for offshore events and in the presence of data gaps, these limitations are now explicitly quantified rather than being hidden within deterministic outputs. Together, these results demonstrate a practical pathway for operationalizing probabilistic source modeling in automated hazard response systems.

Future work will focus on strengthening redundancy for real-time precise products, refining strategies for handling missing data, and propagating uncertainty into downstream hazard-assessment systems.

Abbreviations

CI	Confidence interval
EEW	Earthquake early warning
GEONET	GNSS earth observation network system
GNSS	Global navigation satellite system
GSI	Geospatial Information Authority of Japan
JAXA	Japan Aerospace Exploration Agency
JMA	Japan Meteorological Agency
MCMC	Markov chain monte carlo methods
Mw	Moment magnitude
PDF	Probability density function
PPP	Precise point positioning
REGARD	Real-time GEONET analysis system for rapid deformation monitoring
RTK	Real-time kinematic
RUNE	Real-time automatic uncertainty estimation of source models using crustal-deformation data
VR	Variance reduction

Supplementary Information

The online version contains supplementary material available at https://doi.org/10.1186/s40623-026-02513-9.

Supplementary Material 1.

Authors' information

KO, SA, NT, TM, KY, CS, MH, RY, and SK are staff members of the Geospatial Information Authority of Japan. YO is a professor in the Graduate School of Science at Tohoku University.

Acknowledgements

This study was partly supported by the JST FOREST Program (Grant Number JPMJFR202P, Japan). Additional support was provided by MEXT through the Third Earthquake and Volcano Hazards Observation and Research Program (Earthquake and Volcano Hazard Reduction Research), the Research Project

for Disaster Prevention of Great Earthquakes along the Nankai Trough, and the MEXT Coordination Funds (Grant Number J013348, Japan).

Author contributions
SA, NT, SK and YO designed the study. TM implemented the Precise Point Positioning cluster. KY and CS built and operated the precise orbit and clock estimation subsystem. MH and RY monitored the trial operation. YO developed the model-inversion program. KO contributed to all the above components and implemented the Markov Chain Monte Carlo system.

Funding
This study was partly supported by the JST FOREST Program (Grant Number JPMJFR202P, Japan). Additional support was provided by MEXT through the Third Earthquake and Volcano Hazards Observation and Research Program (Earthquake and Volcano Hazard Reduction Research), the Research Project for Disaster Prevention of Great Earthquakes along the Nankai Trough, and the MEXT Coordination Funds (Grant Number J013348, Japan).

Data availability
All 30-s GEONET raw data are available in the GSI repository. Anyone lives in Japan can access our products and analysis strategy summary files after the user registration at https://terras.gsi.go.jp/ftp_user_regist.php. People in overseas are required to submit an application form that can be downloaded at https://www.gsi.go.jp/ENGLISH/geonet_english.html.

Declarations

Ethics approval and consent to participate
Not applicable.

Consent for publication
Not applicable.

Competing interests
The authors declare that they have no competing interests.

Author details
[1]Geospatial Information Authority of Japan, 1 Kitasato, Tsukuba 305-0811, Japan. [2]Research Center for Prediction of Earthquakes and Volcanic Eruptions, Graduate School of Science, Tohoku University, Sendai, Japan. [3]International Research Institute of Disaster Science, Tohoku University, Aoba 468-1, Aramaki, Aoba-ku, Sendai 980-8572, Japan. [4]Advanced Institute for Marine Ecosystem Change (WPI-AIMEC), Tohoku University, 6-3 Aoba, Aramaki, Aoba-ku, Sendai 980-8578, Japan. [5]Division for the Establishment of Frontier Sciences of Organization for Advanced Studies, Tohoku University, 2-1-1 Katahira, Aoba-ku, Sendai 980-8577, Japan.

Received: 25 March 2026 Accepted: 28 July 2026
Published online: 19 August 2026

References

Agata R, Kasahara A, Yagi Y (2021) A Bayesian inference framework for fault slip distributions based on ensemble modelling of the uncertainty of underground structure: with a focus on uncertain fault dip. Geophys J Int 225(2):1392–1411

Baba T, No T, Obana K, Imai K, Chikasada N, Tanioka Y, Kodaira S (2024) Authentic fault models and dispersive tsunami simulations for outer-rise normal earthquakes in the southern Kuril Trench. Earth Planet Space 76:98. https://doi.org/10.1186/s40623-024-02046-z

Báez JC, Leyton F, Troncoso C, del Campo F, Bevis M, Vigny C, Moreno M, Simons M, Kendrick E, Parra H, Blume F (2018) The Chilean GNSS network: current status and progress toward early warning applications. Seismol Res Lett 89(4):1546–1554. https://doi.org/10.1785/0220180011

Blewitt G, Kreemer C, Hammond WC, Plag H-P, Stein S, Okal E (2006) Rapid determination of earthquake magnitude using GPS for tsunami warning systems. Geophys Res Lett 33:L11309. https://doi.org/10.1029/2006GL026145

Blewitt G, Hammond WC, Kreemer C, Plag H-P, Stein S, Okal E (2009) GPS for real-time earthquake source determination and tsunami warning systems. J Geod 83:335–343. https://doi.org/10.1007/s00190-008-0262-5

CODE Analysis Center (AIUB). 2026. Ultra-rapid orbit and clock products. Astronomical Institute, University of Bern. https://www.aiub.unibe.ch/research/code___analysis_center/index_eng.html. (Accessed 20 Mar 2026)

Dettmer J, Benavente R, Cummins PR, Sambridge M (2014) Trans-dimensional finite-fault inversion. Geophys J Int 199:735–751. https://doi.org/10.1093/gji/ggu280

Furumura T (2014) Radiation and Generation of Short- and Long-Period Ground Motions from the 2011 Off Tohoku, Japan, Mw9.0 Earthquake, J Disaster Res 9:281–293. https://doi.org/10.20965/jdr.2014.p0281

Geyer CJ. 1991. Markov Chain Monte Carlo Maximum Likelihood. In: Computing Science and Statistics, Proceedings of the 23rd Symposium on the Interface. 156–163.

GSI. 2024a. Coseismic fault model of the 2024 Noto Peninsula Earthquake. https://www.gsi.go.jp/common/000255958.pdf. (Accessed 20 Mar 2026)

GSI. 2024b. Coseismic fault model of the 2024 Hyuga-nada Earthquake. https://www.gsi.go.jp/common/000260639.pdf. (Accessed 20 Mar 2026)

GSI. 2025. Coseismic fault model of the 2025 Aomori-Oki Earthquake. https://www.gsi.go.jp/common/000274431.pdf. (Accessed 20 Mar 2026)

Hastings WK (1970) Monte Carlo sampling methods using Markov chains and their applications. Biometrika 57:97–109. https://doi.org/10.2307/2334940

Hennig P, Osborne MA, Girolami M (2015) Probabilistic numerics and uncertainty in computations. The Royal Society

IGS. 2026. IGS RTS Products. International GNSS Service. https://igs.org/rts/user-access/. (Accessed 20 Mar 2026)

Jasra A, Stephens DA, Holmes CC (2007) On population-based simulation for static inference. Stat Comput 17(3):263–279. https://doi.org/10.1007/s11222-007-9028-9

JMA. 2026. https://www.jma.go.jp/jma/en/Activities/earthquake.html. (Accessed 20 Mar 2026)

Kaiser A, Andrews J, Fry B, Horspool N, Lukovic B, Massey C, Smith EW, Chamberlain C, Goded T (2024) Dynamic Shaking Layer models for large New Zealand earthquakes (M6.5+): from rapid source characterization to landslide and impact forecasting. NZSEE

Kawamoto S, Hiyama Y, Ohta Y, Nishimura T (2016) First result from the GEONET real-time analysis system (REGARD): the case of the 2016 Kumamoto earthquakes. Earth Planet Space 68:1–12. https://doi.org/10.1186/s40623-016-0564-4

Kawamoto S, Ohta Y, Hiyama Y, Todoriki M, Nishimura T, Furuya T, Sato Y, Yahagi T, Miyagawa K (2017) REGARD: a new GNSS-based real-time finite fault modeling system for GEONET. J Geophys Res Solid Earth 122:1324–1349. https://doi.org/10.1002/2016JB013485

Kawate K, Igarashi Y, Yamada H, Akiyama K, Okeya M, Takiguchi H, Murata M, Sasaki T, Matsushita S, Miyoshi S, Miyoshi M, Kogure S (2023) MADOCA: Japanese precise orbit and clock determination tool for GNSS. Adv Space Res 71(10):3927–3950. https://doi.org/10.1016/j.asr.2023.01.060

Kiureghian A, Ditlevsen O (2009) Aleatory or epistemic? Does it matter? Struct Saf 31(2):105–112

Kouba J, Héroux P (2001) Precise point positioning using IGS orbit and clock products. GPS Solutions 5:12–28. https://doi.org/10.1007/PL00012883

Larson KM (2009) GPS seismology. J Geod 83(3–4):227–233. https://doi.org/10.1007/s00190-008-0233-x

Larson KM, Bodin P, Gomberg J (2003) Using 1-Hz GPS data to measure deformations caused by the Denali fault earthquake. Science 300:1421–1424. https://doi.org/10.1126/science.1084531

Lin J, Chang W, Melgar D, Thomas A, Chiu C (2019) Quick determination of earthquake source parameters from GPS measurements: a study of suitability for Taiwan. Geophys J Int 219(2):1148–1162. https://doi.org/10.1093/gji/ggz359

Matsu'ura M, Hasegawa Y (1987) A maximum likelihood approach to nonlinear inversion under constraints. Phys Earth Planet Interiors 47:179–187. https://doi.org/10.1016/0031-9201(87)90076-8

Melgar D, Bock Y (2013) Near-field tsunami models with rapid earthquake source inversions from land- and ocean-based observations: the potential for forecast and warning. J Geophys Res Solid Earth 118:5939–5955. https://doi.org/10.1002/2013JB010506

Melgar D, Bock Y, Crowell BW (2012) Real-time centroid moment tensor determination for large earthquakes from local and regional displacement

records. Geophys J Int 188(2):703–718. https://doi.org/10.1111/j.1365-246X.2011.05297.x
Melgar D, Allen RM, Riquelme S, Geng J, Bravo F, Baez JC, Parra H, Barrientos S, Fang P, Bock Y, Bevis M, Caccamise DJ II, Vigny C, Moreno M, Smalley R Jr (2016) Local tsunami warnings: perspectives from recent large events. Geophys Res Lett 43:1109–1117. https://doi.org/10.1002/2015GL067100
Metropolis N, Rosenbluth AW, Rosenbluth MN, Teller AH, Teller E (1953) Equations of state calculations by fast computing machines. J Chem Phys 21:1087–1092
Murray JR, Bartlow N, Bock Y, Brooks BA, Foster J, Freymueller J, Hammond W, Hodgkinson K, Johanson I, López-Venegas A, Mann D, Mattioli G, Melbourne T, Mencin D, Montgomery-Brown E, Murray MH, Smalley R, Thomas V (2019) Regional global navigation satellite system networks for crustal deformation monitoring. Seismol Res Lett 91(2A):552–572. https://doi.org/10.1785/0220190113
Niell AE (1996) Global mapping functions for the atmosphere delay at radio wavelengths. J Geophys Res 101(B2):3227–3246. https://doi.org/10.1029/95JB03048
Ohno K, Ohta Y, Kawamoto S, Abe S, Hino R, Koshimura S, Musa A, Kobayashi H (2021) Real-time automatic uncertainty estimation of coseismic single rectangular fault model using GNSS data. Earth Planet Space 73:127. https://doi.org/10.1186/s40623-021-01425-0
Ohno K, Ohta Y, Hino R, Koshimura S, Musa A, Abe T, Kobayashi H (2022) Rapid and quantitative uncertainty estimation of coseismic slip distribution for large interplate earthquakes using real-time GNSS data and its application to tsunami inundation prediction. Earth Planet Space 74:24. https://doi.org/10.1186/s40623-022-01586-6
Ohno K, Ohta Y, Takamatsu N, Munekane H, Iguchi M (2024a) Real-time modeling of transient crustal deformation through the quantification of uncertainty deduced from GNSS data. Earth Planet Space 73:127. https://doi.org/10.1186/s40623-024-02068-7
Ohno K, Takamatsu N, Akiyama K, Kawate K. 2024b. IGS analysis center in Japan – JGX products operations and prospects, IGS Workshop 2024. https://igs.org/workshop/2024/. (Accessed 20 Mar 2026)
Ohta Y, Meilano I, Sagiya T, Kimata F, Hirahara K (2006) Large surface wave of the 2004 Sumatra-Andaman earthquake captured by the very long baseline kinematic analysis of 1-Hz GPS data. Earth Planet Space 58:153–157. https://doi.org/10.1186/BF03353372
Ohta Y, Kobayashi T, Tsushima H, Miura S, Hino R, Takasu T, Fujimoto H, Iinuma T, Tachibana K, Demachi T, Sato T, Ohzono M, Umino N (2012) Quasi real-time fault model estimation for near-field tsunami forecasting based on RTK-GPS analysis: application to the 2011 Tohoku-Oki earthquake (Mw 9.0). J Geophys Res. https://doi.org/10.1029/2011JB008750
Ohta Y, Inoue T, Koshimura S, Kawamoto S, Hino R (2018) Role of real-time GNSS in near-field tsunami forecasting. J Disaster Res 13:453–459. https://doi.org/10.20965/jdr.2018.p0453
Okada Y (1992) Internal deformation due to shear and tensile faults in a halfspace. Bull Seismol Soc Am 82(2):1018–1040. https://doi.org/10.1785/BSSA0820021018
Ragon T, Sladen A, Simons M (2018) Accounting for uncertain fault geometry in earthquake source inversions-I: theory and simplified application. Geophys J Int 214(2):1174–1190
Ruhl CJ, Melgar D, Chung AI, Grapenthin R, Allen RM (2019) Quantifying the value of real-time geodetic constraints for earthquake early warning using a global seismic and geodetic data set. J Geophys Res Solid Earth 124:3819–3837. https://doi.org/10.1029/2018JB016935
Saastamoinen J (1972) Atmospheric correction for the troposphere and stratosphere in radio ranging of satellites. Use Artif Satell Geodesy 15:247–251. https://doi.org/10.1029/GM015p0247
Sagiya T (2004) A decade of GEONET: 1994–2003 the continuous GPS observation in Japan and its impact on earthquake studies. Earth Planet Space. https://doi.org/10.1186/BF03353077
Tanaka Y, Ohta Y, Miyazaki S (2019) Real-time coseismic slip estimation via the GNSS carrier phase to fault slip approach: a case study of the 2016 Kumamoto earthquake. Geophys Res Lett 46(3):1367–1374
Tsuji H, Hatanaka Y (2018) GEONET as infrastructure for disaster mitigation. J Disaster Res 13:424–432. https://doi.org/10.20965/jdr.2018.p0424
Yamada T, Ohta Y, Nishimura T, Yoshida K, Hiramatsu Y, Kinoshita Y (2025) Coseismic slip distribution of the 2024 Noto Peninsula earthquake deduced from dense global navigation satellite system network and interferometric synthetic aperture radar data: effect of assumed dip angle. Earth Planet Space 77:19. https://doi.org/10.1186/s40623-025-02154-4
Zumberge JF, Heflin MB, Jefferson DC, Watkins MM, Webb FH (1997) Precise point positioning for the efficient and robust analysis of GPS data from large networks. J Geophys Res Solid Earth 102(B3):5005–5017. https://doi.org/10.1029/96JB03860

Publisher's Note

Springer Nature remains neutral with regard to jurisdictional claims in published maps and institutional affiliations.